Journal of Power Sources 279 (2015) 439–449

Contents lists available at ScienceDirect

Journal of Power Sources

journal homepage: www.elsevier.com/locate/jpowsour

State of charge estimation for $LiMn_2O_4$ power battery based on strong tracking sigma point Kalman filter

Di Li [a], Jian Ouyang [a, *], Huiqi Li [b], Jiafu Wan [a]

[a] School of Mechanical and Automotive Engineering, South China University of Technology, Guangzhou 510640, China
[b] Guangzhou Electric Vehicle Co. Ltd, Guangzhou 511442, China

HIGHLIGHTS

- A battery model was built for the estimation of the battery State of Charge (SOC).
- Test data of battery was used to obtain accurate parameters for the battery model.
- A improve Sigma Point Kalman Filtering (SPKF) algorithm was used to estimate the SOC.
- Strong Tracking Factor was used to enhance the accuracy of the SPKF algorithm.
- Adequate experimental and simulated data based on the improve SPKF were discussed.

ARTICLE INFO

Article history:
Received 13 March 2014
Received in revised form
22 November 2014
Accepted 1 January 2015
Available online 2 January 2015

Keywords:
Equivalent circuit model
Strong tracking sigma point Kalman filtering algorithm
State of charge estimation
Battery management system
Lithium-ion battery

ABSTRACT

The State of Charge (*SOC*) estimation is important since it has a crucial role in the operation of Electrical Vehicle (EV) power battery. This paper built an Equivalent Circuit Model (*ECM*) of the $LiMn_2O_4$ power battery, and vast characteristics experiments were undertaken to make the model identification and thus the battery *SOC* estimation was realized. The *SOC* estimation was based on the Strong Tracking Sigma Point Kalman Filter (STSPKF) algorithm. The comparison of experimental and simulated results indicates that the STSPKF algorithm performs well in estimating the battery *SOC*, which has the advantages of tracking the variables in real-time and adjusting the error covariance by taking the Strong Tracking Factor (STF) into account. The results also show that the STSPKF algorithm estimated the *SOC* more accurately than the Extended Kalman Filter (EKF) algorithm.

1. Introduction

As concerns for global warming and depletion of natural resources continue to grow, the Electric Vehicles (EVs) are establishing as the most promising solution to the increasing problems associated with the transportation. The internal combustion engines based automobile industry is gradually transitioning to EVs [1] and Hybrid Electric Vehicles (HEVs). These EVs taking advantage of the renewable sources of electricity have been widely accepted as important transitional technologies for sustainable transportation [2].

The power battery is an important component of EVs and HEVs and plays a crucial role in their successful application. Among the various types of power batteries, the Lithium-ion battery possesses the higher energy to weight ratio and long operating life, which is recognized as the most promising for EV applications. However, due to its unique characteristics, the Lithium-ion power battery must be used with the support of Battery Management System (BMS) to ensure safe and reliable operations. The BMS should prevent over-discharging or over-charging under all operating conditions, extend the lifetime and protect the battery from permanent damage thereby facilitating its safe and efficient discharging and charging [3]. The functions of BMS include the battery parameter measurement, State of Charge (*SOC*) estimation, safety management, battery pack equilibrium, thermal management, etc. The *SOC* is defined as the ratio of capacity at a given time to the nominal capacity of the battery [4]. The estimation of *SOC* is one of the most important functions of BMS.

* Corresponding author.
E-mail address: jim_oyoung@163.com (J. Ouyang).

http://dx.doi.org/10.1016/j.jpowsour.2015.01.002
0378-7753/

Generally, the *SOC* estimation methods can be divided into two categories. The first category is based on the direct measurement, in which the *SOC* is estimated by a simple relationship between the measurements and the *SOC*. In our view, the following methods belong to this category. 1) The discharge test is the most reliable method under the laboratory conditions. However, it is too time-consuming and hard to use in practice. 2) The open-circuit voltage is a promising method in applications with relatively long rest periods. Since the rest periods will occur only occasionally, it is used in combination with other techniques for ensuring continuous indication of the *SOC* [5]. 3) The ampere hour counting (current integration) method has been widely used, which has reasonable accuracy and is cost effective when a sufficiently accurate current sensor is adopted. This method was reported to have several drawbacks [6–8]. It fails to estimate coulombic efficiency accurately, determine the initial *SOC*, or indicate the variations in initial *SOC* resulting from self-discharge and other factors. In addition, the error becomes large when the battery operates at high and low temperature or when the current sharply fluctuates. Also, it is an open loop *SOC* estimator that will accumulate the error [9].

The second category combines the battery model, measurement data and control algorithm. As a whole, there are the following four types of battery models to describe the functioning and operation of the battery:

1) The electrochemical model, which describes the internal reactions of the battery by adopting a certain mathematical equation. Reinhardt Klein et al. presented a full macro-homogeneous 1-D model of a Li-ion battery as well as its reduction, suitable for the purpose of estimation and control [10]. MengGuo et al. designed a multi-geometry and physical model for Li-ion battery module [11], which predicts 3-D profiles of the electrical potential and temperature in the battery. However, the electrochemical model is too complicated for most practical applications.
2) The specific factor model is designed for describing a specific factor (e.g., temperature model, and cycle life model) of the battery. Quanshi Chen et al. proposed the temperature model which could describe the decrease in battery capacity with decreasing temperature without the knowledge of best working temperature [12]. The authors also gave a relationship between the cycle life and the depth of discharge. However, one specific factor model can only describe one aspect of the battery.
3) The Electrochemical Impedance Spectroscopy (EIS) model is on the basis of an experimental method that characterizes electrochemical systems of the battery. The amplitude and phase of electrochemical impedance are measured when a small AC current flows through the battery. The EIS also can be obtained by repeating this procedure for a certain range of frequencies [13]. It is a unique technique for the analysis of the very slow dynamics of the batteries [14]. In Refs. [14–19] the authors used several methods to build the EIS models, and based on them estimated the *SOC* of the battery.
4) The Equivalent Circuit Model (*ECM*) is an external characteristic model that can be used to predict battery behavior [20]. The *ECM*'s mathematical expression as transfer functions could be introduced to describe only the behavior of the input and output variables of the battery, such as current and voltage [21]. The *ECM* generally includes an *n*th-order *RC* network to simulate the battery behavior, and offers best compromise between the time for computations, parameterization effort, and precision of the simulation [22]. A first-order *RC* network was used to simulate the battery [23–25], which saved the computational time but lacked accuracy. Low Wen Yao et al. compared the first-, second-, and third-order *RC* networks, reducing the complexity of battery modeling and multi-cell analysis [26]. Their studies also show that notable modeling error existed in the relaxation effect modeling when first-order *RC* network is applied, and that the accuracy improved when second- or third-order *RC* network is used. The prediction of battery behavior using *n*th-order *RC* network was also discussed in Refs. [27–29]. It can be concluded that increasing the *RC* networks, subjected to *n*th-order not exceeding 5th improves the precision of dynamic voltage estimation. At higher values of *n*th, a large error will arise from the linear discrete method. In addition, the excessive computational costs caused by the complex structure of the model make this method unsuitable for nonlinear parameters' identification [28].

Currently, several combinations of battery models and adaptive control algorithms are used in battery characteristics research, such as the *SOC* estimation and state of health evaluation. Several control algorithms, such as the Artificial Neural Network (ANN), fuzzy logic, Support Vector Machine (SVM), and system filtering theory, have been used to estimate the *SOC*. The ANN was first used for depicting the available capacity, estimating the *SOC*, and describing the non-linear relationships in a lead-acid battery [30–34]. Since the degree of battery degradation was used as one of the input signals, this model showed accurate results for batteries of different sizes and degradation states [34]. Another control algorithm is fuzzy logic. It was applied for estimating the battery *SOC* [35–37] based on the training datasets obtained from impedance spectroscopy, coulomb counting techniques, and voltage recovery measurements. Finally, the SVM was also used successfully to estimate the battery *SOC* [38–42]. While the SVM model gives good accuracies, its disadvantages are the offline establishment and heavy computational training processes.

Compared to the above methods, the system filtering theory has the advantages of being closed-loop and real-time, which has attracted the wide attention recently. The widely used system filtering theory is Kalman Filter (KF). However, as KF are linear in filtering process, several modifications have been proposed for their applications to non-linear battery system. Saeed Sepasi et al. established the Extended Kalman Filter (EKF) algorithm [43–48] and Rui Xiong et al. designed the Adaptive EKF algorithm [49–51]. Both of the two methods, which are based on the non-linear state-space functions with first-order Taylor accuracy, are used to estimate the *SOC* of Li-ion battery. However, the EKF has several shortcomings. For example, it has highly unstable characteristics during the linearization when the assumption of local linearity is in violation [52]. Additionally, the derivation of the Jacobian matrices is nontrivial and error-prone in many applications [53]. Consequently, as an alternative approach to the state estimation for non-linear systems, the Sigma Point Kalman Filter (SPKF), which overcomes the theoretical limitations of EKF algorithm, was proposed. This method has at least second-order Taylor accuracy. The Refs. [1,2,53–55] proposed the SPKF method used for estimating the *SOC* of the battery, and demonstrated that SPKF method has more accuracy than EKF method in estimating the *SOC* of the battery.

This paper will adopt the combination of *ECM* and Strong Tracking Sigma Point Kalman Filter (STSPKF) algorithm to estimate the *SOC* of $LiMn_2O_4$ power battery. The STSPKF algorithm as a improve algorithm of SPKF has many advantages, e.g. requires less computation, the system nonlinear function can be a discontinuous function, the measured online error can be adjusted for dynamic *SOC* estimation.

The remainder of this paper is organized as follows. The Section 2 conducts the power battery characteristics experiments. The Section 3 builds an *ECM* for the $LiMn_2O_4$ power battery, describes its application scenarios and uses the experimental data to identify

the *ECM* parameters. The Section 4 proposed the STSPKF algorithm. The Section 5 discusses the simulated results of the proposed algorithm and the experimental data. The Section 6 gives our conclusions.

2. Battery characteristics experiments

2.1. Test bench

For studying the characteristics of the $LiMn_2O_4$ power battery, the battery test bench shown in Fig. 1 was used. The experimental setup consisted of a digatron Battery Testing System (BTS), a thermal chamber with temperature control, a host computer to run the battery testing software, and an experimental battery. The software running on the host computer records the battery data include current, voltage, ampere-hour (Ah), and temperature etc. The digatron BTS can charge/discharge the battery based on a previously designed program with a maximum voltage of 100 V and maximum charging/discharging current of 200 A. The errors of the current and voltage sensors are within 0.5% and 0.1%, respectively. In addition, all of modules in the BTS have a low-pass filtering function incorporated for implementing large noise cancellation. With the given sampled current and voltage, the battery SOC experimental data could be obtained by the designed algorithm of the BTS management module.

2.2. Test procedure

The power battery characteristics test was based on the chapter 4 of the book "Electric Vehicle Power Battery Management System Design" [56]. Based on the method in Ref. [56], Fig. 2 shows the power battery test procedure. At First, the power battery was discharged at 0.02 C-rate to reach its lower cut-off voltage followed by 2 h resting to allow the internal chemical reactions reaching equilibrium state. Secondly, the power battery was charged and discharged with a constant current, both was followed by 2 h resting. Then, the Hybrid Pulse Power Characterization (HPPC) test was performed followed by another 2 h' resting. Finally, Federal Urban Driving Test (FUDS) and Dynamic Stress Test (DST) tests were performed on EV to obtain the operational data. During the test, the battery's operating temperature was maintained at 25 °C.

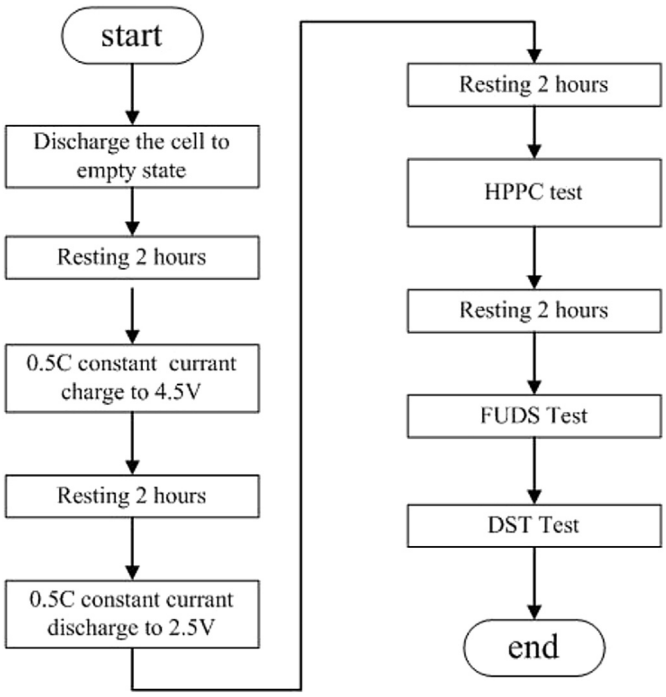

Fig. 2. The battery test procedure.

2.3. Test results

Fig. 3 depicts the graph between the charging/discharging and resting output voltage and time. The experiment was carried out in two stages. The first one was the constant current charge/discharge stage, during which the power battery was charged/discharged to its upper/lower cut-off voltage with a 0.5 C-rate constant current. The second stage was a two-hour resting stage. From the power battery constant current charge/discharge data, the battery's voltage range varies from 3.0 V to 4.5 V, the change of voltage is not obvious in the voltage plateau (corresponding to 10%–90% *SOC*), while the voltage drops rapidly beyond the voltage plateau. The figure shows that the power battery voltage graph showed

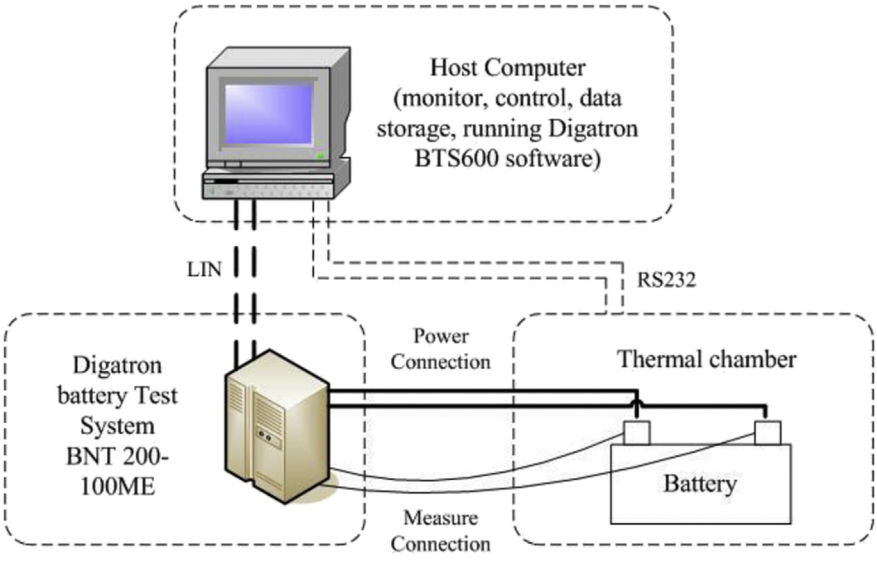

Fig. 1. The battery test bench.

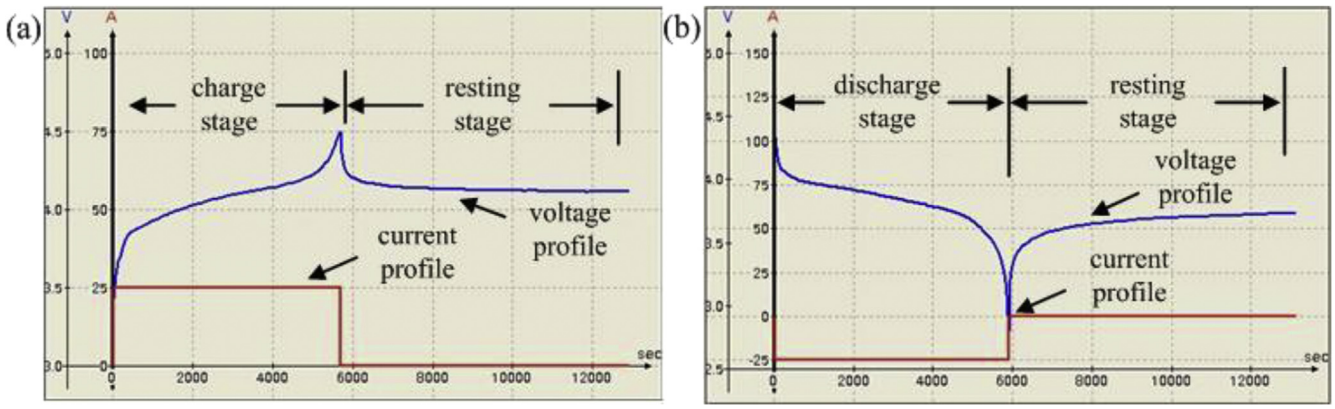

Fig. 3. The graph for constant current charge, discharge and 2-h resting: (a) 0.5 C-rate constant charge and 2-h resting; (b) 0.5 C-rate constant discharge and 2-h resting.

tendency to flatten between 3.8 V and 4.1 V during the charging stage in Fig. 3(a) and between 4.0 V and 3.7 V during the discharging stage in Fig. 3(b).

Fig. 4 shows the HPPC test, at the beginning of the HPPC test, the battery unit was conditioned by charging it approximately to the full capacity and balancing it with a small overcharge. After determining the capacity of the battery, it was charged back to 100% SOC (based on the measured true capacity) and the test was performed.

The current profile of battery HPPC test is shown in Fig. 4(a). The HPPC test was divided into a discharge stage, resting stage and a charge stage [57]. One HPPC cycle includes three stages: the first is 1 C-rate discharge lasting for 10 s; the second is the resting stage lasting for 40 s and the third is 0.75 C-rate charge lasting for 10 s Fig. 4(b) shows the voltage profile of HPPC test. In this study, the HPPC test consisting of ten cycles was performed.

The FUDS and DST are the classical working conditions as specified in the "USABC Electric Vehicle Battery Test Manual" [58]. The sampled current and voltage during eight FUDS current cycles and twenty-nine DST cycles are shown in Fig. 5; the lower and upper lines (in the web version) respectively denote the current and voltage responses. The discharging current is positive and the charging current is negative. That means both discharging and charging processes existed in the FUDS and DST test. However, the general descending trend of the battery voltage indicates that the FUDS and DST test mainly discharged the battery.

The constant current test data was used for comparisons between the simulation results. The HPPC test data was used for *ECM* parameters identification. The FUDS and DST tests reflect the performance of power battery used in the EVs. These experimental data can be applied to identify the parameters of the power battery.

3. Battery modeling

3.1. Physical and mathematical description of the battery

To estimate the *SOC*, a model for the battery is necessary. A variety of battery models are developed to obtain Li-ion battery performance for various applications [59]. The model used in this study was based on an equivalent circuit with the polarization characteristics simulated by the *RC* network. Since a difference between concentration polarization and electrochemical polarization exists, an *ECM* is presented in Fig. 6. This model is defined as the dual polarization model and it refines the description of polarization characteristics. In addition, it simulates the concentration polarization and the electrochemical polarization separately [60].

In Fig. 6 *EMF* means the Electromotive Force and its relationship with *SOC* is denoted by an explicit function. R_o is the internal Ohmic resistance. The *RC* network (R_{p1},R_{p2},C_{p1},C_{p2}) is used to simulate the relaxation effect of the battery. I_L and U_{oc} represent the load current and the open circuit voltage, respectively. In actual applications, U_{oc} is the load voltage.

According to the Kirchhoff voltage laws, the model can be expressed as follows:

$$U_{oc} = EMF - I_L R_o - U_{p1} - U_{p2} \tag{1}$$

$$\dot{U}_{p1} = -\frac{U_{p1}}{R_{p1}C_{p1}} + \frac{I_L}{C_{p1}} \tag{2}$$

$$\dot{U}_{p2} = -\frac{U_{p2}}{R_{p2}C_{p2}} + \frac{I_L}{C_{p2}} \tag{3}$$

$$SOC(k) = SOC(0) + \frac{\int_0^k \eta_i I_L(t)\mathrm{d}t}{C_N} \tag{4}$$

where$SOC(0)$ is the initial *SOC*; $SOC(k)$ is the current *SOC* at time k; C_N is the battery nominal capacity; $I_L(t)$ is the current at time t and η_i is the coulombic efficiency.

3.2. Application scenarios of the battery

The battery (extreme left in Fig. 7) used in this study was a $LiMn_2O_4$ power battery (PL60110190) with a nominal capacity of 50 Ah and 185 Wh. It was manufactured by a new energy technology co. in Zhejiang Province of People's Republic of China. The $LiMn_2O_4$ power battery has a higher voltage platform than that of other Li-ion batteries. It is especially suitable for EV application because it has less number of cells for the same total voltage, thereby reducing the weight of the vehicle. The nominal voltage of the power battery pack, which consisted of 16 batteries connected in series (center of Fig. 7), was 60 V. Each battery equipped with an active equilibrium module to ensure the output voltage and the capacity remain constant during operation, so the number of equilibrium module is 16 in total for a battery pack. The EV (extreme right of Fig. 7), which used the power battery pack as the power source, was designed for short-distance transportation. With a gross weight of 180 kg and a maximum grade ability of 22%, it reached a speed greater than 60 km/h and a driving range of more than 60 km.

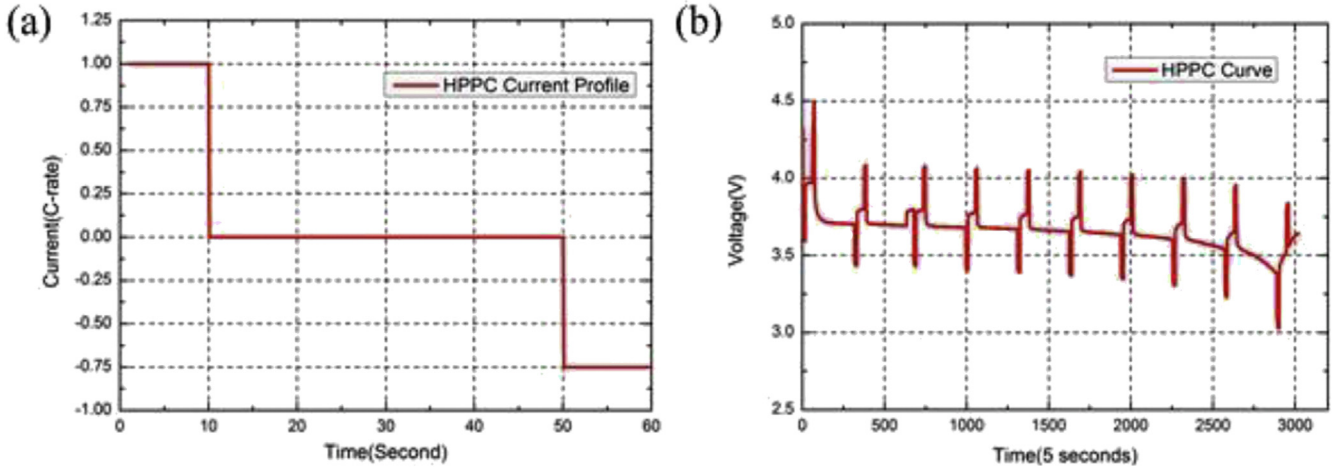

Fig. 4. The battery HPPC test: (a) Current Profile; (b) Voltage Profile.

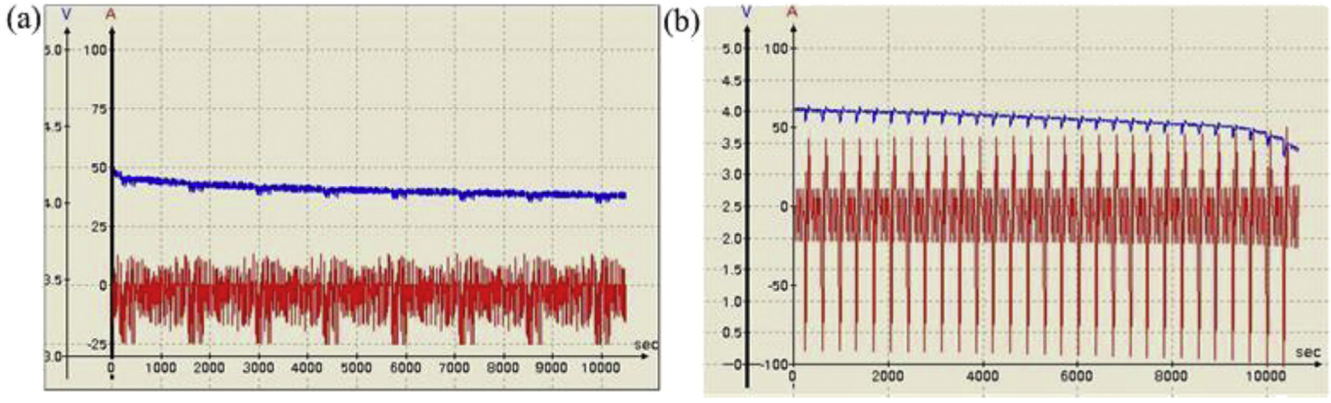

Fig. 5. The profiles of current and voltage in FUDS and DST test: (a) FUDS test; (b) DST test.

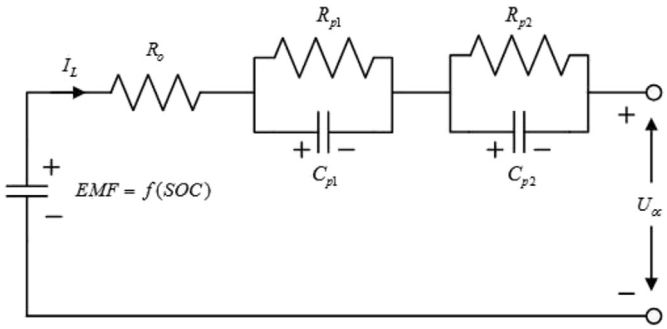

Fig. 6. The *ECM* of the battery.

3.3. Parameters identification

In this paper, two categories of parameters, namely the parameters of function $EMF = f(SOC)$ and the parameters,R_{p1},R_{p2},C_{p1},C_{p2},R_o of the *ECM* expression are needed to be identified.

3.3.1. The parameters identification method

1) The method for $EMF = f(SOC)$ parameters

In actual application, the battery's *SOC* is always limited to remain within 10%–90% range to protect it from any damage. In this study, the least square method is used to identify the parameters of

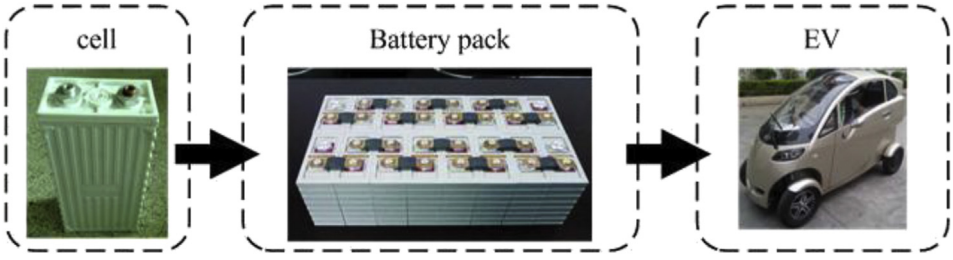

Fig. 7. The $LiMn_2O_4$ Power battery, Power battery pack and EV.

$EMF = f(SOC)$ function with the condition when the SOC lies from 10% to 90% that of power battery.

For the least square method theory, if the function space Φ is similar to linear function then it can be equaled to $P_n = Span\{1,x,\cdots,x^n\}$. Supposing $s(x) \in P_n$, $s(x)$ can be written in the form (5)

$$s(x) = a_0 + a_1 x + \ldots + a_n x^n \tag{5}$$

Assuming that $s(x)$ is chosen, the objective here is to solve outs$^*(x)$ based on the given data.

The equation (6) is set to obtain the parameters$a_0,a_1,\ldots,a_n$.

$$\sum_{j=0}^{m} \rho(x_j)\left[f(x_j) - s^*(x_j)\right]^2 = \min \sum_{j=0}^{m} \rho(x_j)\left[f(x_j) - \sum_{i=0}^{n} a_i \varphi_i(x_j)\right]^2 \tag{6}$$

According to the equations (5) and (6), the parameters of $EMF = f(SOC)$ can be identified by the equations (7) and (8):

$$EMF = a_0 + a_1 SOC + a_2 SOC^2 + a_3 SOC^3 \tag{7}$$

Nine SOC points in this range were chosen in the voltage plateau area (from 3.7 V to 4.1 V) of the constant current discharge graph (Fig. 3(b)) for parameters identification of $EMF = f(SOC)$. Table 1 shows the experimental data for identification of parameters for $EMF = f(SOC)$.

2) The method for ECM parameters

Hysteresis effect was observed in the voltage experiments conducted on the power battery. When the battery switches from charge or discharge state, the sudden change of current causes the voltage to change through large magnitude due to the ohmic resistance. In the resting period however, the voltage changes slowly because of the electrochemical effect of the internal battery. This phenomenon and the experimental data can be used to identify the ohmic and the polarization resistance. The HPPC voltage response curve for a period is shown in Fig. 8, while there appears the curve of ten periods in Fig. 4 (b). The current profile corresponding to each period of the voltage response curve is shown in Fig. 4 (a), containing 1C discharge and 0.75C charge currents.

In this study, a genetic algorithm is used to find the optimal value of τ_1, τ_2 and the objective function of the genetic algorithm is established as follows: [60].

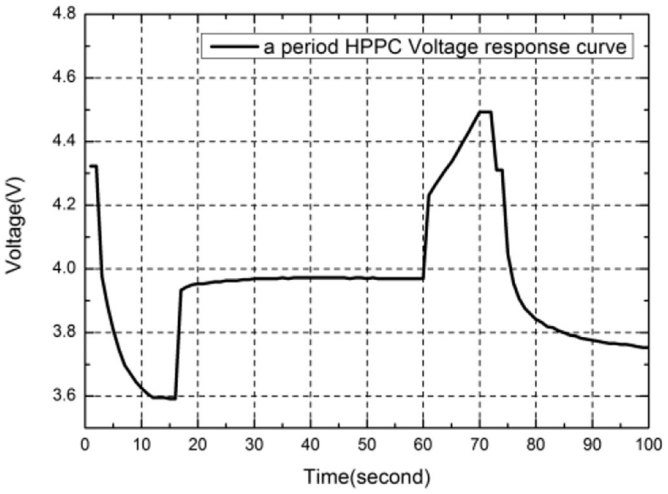

Fig. 8. The diagram of a period HPPC voltage response curve.

$$\begin{cases} \min\left\{f\left(\hat{\chi}_k^{(g)}\right)\right\} \\ f\left(\hat{\chi}_k^{(g)}\right) = \dfrac{1}{N}\sum_{i=1}^{N}\left(U_{oc,k} - \hat{U}_{oc,k}\left(\hat{\chi}_k^{(g)}\right)\right)^2 \end{cases} \tag{9}$$

where, $\hat{\chi}_k^{(g)}$ is the estimation value of current population χ_k at generationg; χ_k is the current individual k of the population χ, where $\chi = \begin{bmatrix} \tau_1 & 0 \\ 0 & \tau_2 \end{bmatrix}$; $\hat{U}_{oc,k}$ is the estimation value of U_{oc} at the individual k; N is the estimation length.

Regression equation (10) are used for identification of parameters for ECM expression:

$$\begin{cases} (1,1)a_0 + (1,SOC)a_1 + \left(1,SOC^2\right)a_2 + \left(1,SOC^3\right)a_3 = (1,EMF) \\ (SOC,1)a_0 + (SOC,SOC)a_1 + \left(SOC,SOC^2\right)a_2 + \left(SOC,SOC^3\right)a_3 = (SOC,EMF) \\ \left(SOC^2,1\right)a_0 + \left(SOC^2,SOC\right)a_1 + \left(SOC^2,SOC^2\right)a_2 + \left(SOC^2,SOC^3\right)a_3 = \left(SOC^2,EMF\right) \\ \left(SOC^3,1\right)a_0 + \left(SOC^3,SOC\right)a_1 + \left(SOC^3,SOC^2\right)a_2 + \left(SOC^3,SOC^3\right)a_3 = \left(SOC^3,EMF\right) \end{cases} \tag{8}$$

Table 1
Experimental data for identification of parameters for $EMF = f(SOC)$.

SOC	0.9	0.8	0.7	0.6	0.5	0.4	0.3	0.2	0.1
EMF	4.059	3.99	3.964	3.934	3.898	3.862	3.833	3797	3.754

3.3.2. Parameters identification results

Parameters identification results for $EMF = f(SOC)$ and ECM are shown in Table 2 and Table 3, respectively.

4. *SOC* estimation based on the STSPKF algorithm

KF is a well-known estimation theory, It was introduced in 1960 [61]. It provides a recursive solution to estimate systems' state variables through a linear optimal filtering [44]. For non-linear systems, the SPKF as an alternative approach is widely used to the state estimation. The STSPKF based method adopted in this paper is an improvement of the SPKF.

The STSPKF method based on a nonlinear system state space equation can be stated as follows.

$$\begin{cases} U_{oc,i} = EMF - I_{L,i}R_o - I_{p1,i}R_{p1} - I_{p2,i}R_{p2} \\ I_{p1,i} = \left(1 - \dfrac{\left(1 - e^{-\frac{\Delta t}{\tau_1}}\right)}{\dfrac{\Delta t}{\tau_1}}\right) I_{L,i} + \left(\dfrac{1 - e^{-\frac{\Delta t}{\tau_1}}}{\dfrac{\Delta t}{\tau_1}} - e^{-\frac{\Delta t}{\tau_1}}\right) I_{L,i-1} + e^{-\frac{\Delta t}{\tau_1}} I_{p1,i-1} \\ I_{p2,i} = \left(1 - \dfrac{\left(1 - e^{-\frac{\Delta t}{\tau_2}}\right)}{\dfrac{\Delta t}{\tau_2}}\right) I_{L,i} + \left(\dfrac{1 - e^{-\frac{\Delta t}{\tau_2}}}{\dfrac{\Delta t}{\tau_2}} - e^{-\frac{\Delta t}{\tau_2}}\right) I_{L,i-1} + e^{-\frac{\Delta t}{\tau_2}} I_{p2,i-1} \end{cases} \quad (10)$$

$$\begin{cases} x_k = f_{k-1}(x_{k-1}) + \omega_{k-1} \\ z_k = h_k(x_k) + \nu_k \end{cases} \quad (11)$$

where x_k is the state variable, f_{k-1} is the nonlinear state function, ω_{k-1} is the system process noise, z_k is the measured variable, h_k is the nonlinear measured function, and ν_k is the measured noise, the ω_{k-1} and ν_k must satisfy the equation (12):

$$\begin{cases} E(\omega_k) = q_k, Cov(\omega_k, \omega_j) = Q_k\delta_{kj} \\ E(\nu_k) = r_k, Cov(\nu_k, \nu_j) = R_k\delta_{kj} \\ Cov(\omega_k, \nu_j) = 0 \end{cases} \quad (12)$$

4.1. Initialization

The deterministic discrete-time state equations to the battery *ECM* can be described by the equation (13):

$$\begin{cases} SOC(k) = SOC(k-1) + \dfrac{\eta(k)\Delta t}{C_N} I_L(k) \\ U_{p1}(k) = U_{p1}(k-1)e^{-\frac{\Delta t}{\tau_1}} + I_L(k-1)R_1\left(1 - e^{-\frac{\Delta t}{\tau_1}}\right) \\ U_{p2}(k) = U_{p2}(k-1)e^{-\frac{\Delta t}{\tau_2}} + I_L(k-1)R_2\left(1 - e^{-\frac{\Delta t}{\tau_2}}\right) \\ U_{oc}(k) = EMF(SOC(k)) - I_L(k)R_o - U_{p1}(k) - U_{p2}(k) \end{cases} \quad (13)$$

A state vector is defined as follows:

$$X = \begin{pmatrix} SOC \\ U_{p1} \\ U_{p2} \end{pmatrix} \quad (14)$$

The initial state mathematical expectation and covariance is:

$$\begin{cases} \hat{x}_0 = E(x_0) \\ P_0 = Var(x_0) = E\left((x_0 - \hat{x}_0)(x_0 - \hat{x}_0)^T\right) \end{cases}$$

The initial process noise covariance is Q_0.
The initial measurement noise covariance is R_0.

Table 2
Parameter identification results for $EMF = f(SOC)$.

a_0	a_1	a_2	a_3
3.6977	0.6138	−0.6733	0.4781

4.2. State vector update

The STSPKF algorithm consists of time updates, measurement

Table 3
Results for identification of parameters for *ECM* results.

$R_o(\Omega)$	$C_{p1}(F)$	$R_{p1}(\Omega)$	$C_{p2}(F)$	$R_{p2}(\Omega)$	τ_1	τ_2
0.02404	5665	0.000645	5404.7	0.008315	3.65	44.9

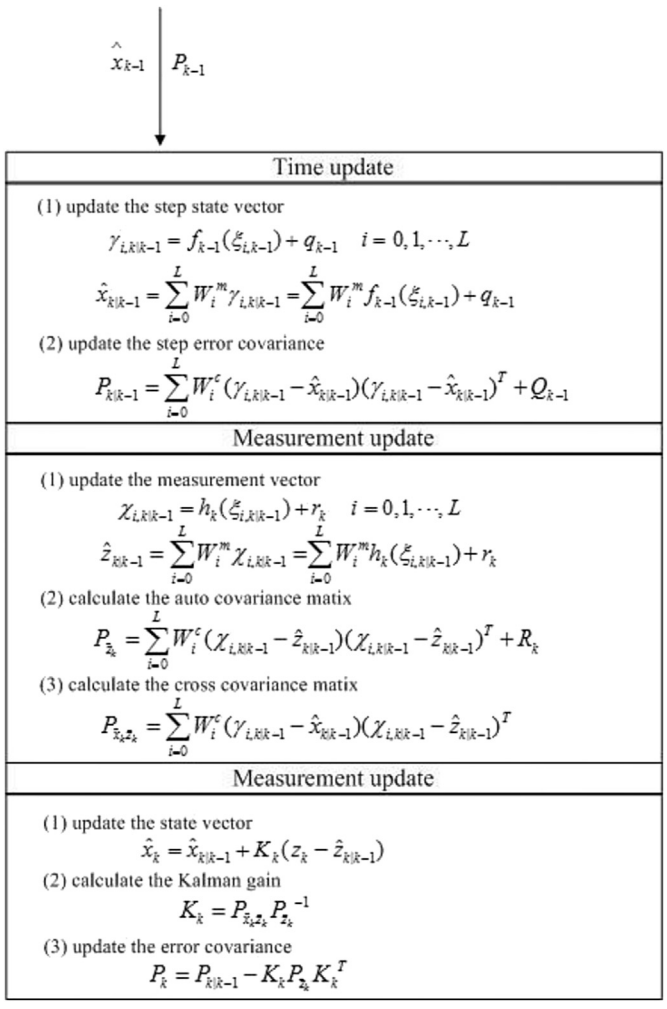

Fig. 9. STSPKF algorithm.

updates and filtering measurement updates, which are summarized in Fig. 9. The figure also gives stepwise computations of the STSPKF based *SOC* estimation algorithm using the *ECM*.

4.2.1. Generating sigma points at time point (k−1)

The paper adopts proportional amendment symmetry sampling strategy, of which $L = 2n$(n denotes system dimension) is picked up and the number of sigma points is $(2n + 1)$. The sigma points and the weight factor can be described by the following expressions:

$$\begin{cases} \xi_{0,k-1} = \overline{x}_{k-1} \\ \xi_{i,k-1} = \overline{x}_{k-1} + \left(\sqrt{(n+\lambda)P_{k-1}}\right)_i \\ \xi_{i+n,k-1} = \overline{x}_{k-1} - \left(\sqrt{(n+\lambda)P_{k-1}}\right)_i \end{cases} \tag{15}$$

where,$\overline{x}_{k-1}$ is the mathematical expectation of $(k-1)$th time point; P_{k-1} is $(k-1)$th time point covariance; $\left(\sqrt{(n+\lambda)P_{k-1}}\right)_i$ is$i$th row of $(n + \lambda)P_{k-1}$'s square root matrix; $\xi_i(i = 0,1,\ldots,2n)$ denotes the ith sigma point and the corresponding weight factors are:

$$W_i^m = \begin{cases} \lambda/(n+\lambda) & i = 0 \\ 1/[2(n+\lambda)] & i \neq 0 \end{cases} \tag{16}$$

$$W_i^c = \begin{cases} \lambda/(n+\lambda) + 1 + \beta - \alpha^2 & i = 0 \\ 1/[2(n+\lambda)] & i \neq 0 \end{cases} \tag{17}$$

$$\lambda = \alpha^2(n+\theta) - n \tag{18}$$

where, W_i^m and W_i^c are the weight factors for solving the first-order and second-order statistical characteristics. α is a positive proportional scaling factor with a range of 0–1. β is a non-negative factor that can be used to adjust the covariance accuracy, with the best value of 2 for the Gaussian distribution. θ is the proportional factor which can be used to adjust the distance between a sigma point and the mathematical expectation $\overline{x}$ generally satisfying the equation $n + \theta = 3$.

4.2.2. Time updates

The time update process includes updating the step state vector and its error covariance (see Fig. 9). In equation (19), sigma point $\xi_{i,k-1}$ generated at $(k-1)$th time point is used to calculate $\gamma_{i,k|k-1}$ by using the non-linear function f_{k-1}. Step mathematical expectation $\widehat{x}_{k|k-1}$ and step error covariance $P_{k|k-1}$ are calculated by using the W_i^m, W_i^c and γ_i, given by equations (20) and (21), separately.

$$\gamma_{i,k|k-1} = f_{k-1}(\xi_{i,k-1}) + q_{k-1} \quad i = 0,1,\ldots,L \tag{19}$$

$$\widehat{x}_{k|k-1} = \sum_{i=0}^{L} W_i^m \gamma_{i,k|k-1} = \sum_{i=0}^{L} W_i^m f_{k-1}(\xi_{i,k-1}) + q_{k-1} \tag{20}$$

$$P_{k|k-1} = \sum_{i=0}^{L} W_i^c \left(\gamma_{i,k|k-1} - \widehat{x}_{k|k-1}\right)^T + Q_{k-1} \tag{21}$$

4.2.3. Generating sigma points at step $k|k-1$

The process of generating sigma points at the step $k|k-1$ is similar to the time point $(k-1)$th.

$$\begin{cases} \xi_{0,k|k-1} = \overline{x}_{k|k-1} \\ \xi_{i,k|k-1} = \overline{x}_{k|k-1} + \left(\sqrt{(n+\lambda)P_{k|k-1}}\right)_i \\ \xi_{i+n,k|k-1} = \overline{x}_{k|k-1} - \left(\sqrt{(n+\lambda)P_{k|k-1}}\right)_i \end{cases} \tag{22}$$

4.2.4. Measurement updates

Measurement update process includes updating of the step measurement vector$\widehat{z}_{k|k-1}$, the error covariance $P_{\tilde{z}_k}$, and the error cross covariance$P_{\tilde{x}_k\tilde{z}_k}$. In equation (23), the sigma point $\xi_{i,k|k-1}$ generated at time step $k|k-1$ is used to calculate the result $\chi_{i,k|k-1}$ obtained through non-linear function h_k. The step measurement vector $\widehat{z}_{k|k-1}$, the error covariance $P_{\tilde{z}_k}$, and the error cross covariance $P_{\tilde{x}_k\tilde{z}_k}$ are calculated using weight factors W_i^m, W_i^c, χ_i, ξ_i and $\widehat{z}_{k|k-1}$ given by the equations 24–26.

$$\chi_{i,k|k-1} = h_k\left(\xi_{i,k|k-1}\right) + r_k \quad i = 0,1,\ldots,L \tag{23}$$

$$\widehat{z}_{k|k-1} = \sum_{i=0}^{L} W_i^m \chi_{i,k|k-1} = \sum_{i=0}^{L} W_i^m h_k\left(\xi_{i,k|k-1}\right) + r_k \tag{24}$$

$$P_{\tilde{z}_k} = \sum_{i=0}^{L} W_i^c \left(\chi_{i,k|k-1} - \widehat{z}_{k|k-1}\right)\left(\chi_{i,k|k-1} - \widehat{z}_{k|k-1}\right)^T + R_k \tag{25}$$

$$P_{\tilde{x}_k\tilde{z}_k} = \sum_{i=0}^{L} W_i^c (\gamma_{i,k|k-1} - \widehat{x}_{k|k-1})\left(\chi_{i,k|k-1} - \widehat{z}_{k|k-1}\right)^T \tag{26}$$

4.2.5. Filtering measurement updates

The filtering measurement update process includes updating the kth point state vector$\widehat{x}_k$, the Kalman gain K_k and the kth point error covariance P_k shown in Fig. 9. In equation (27), step mathematical expectation$\widehat{x}_{k|k-1}$, Kalman gain K_k, measurement data z_k, and step measurement vector $\widehat{z}_{k|k-1}$ are used for calculating the kth point state vector $\widehat{x}_k$. The Kalman gain K_k is calculated using the error covariance $P_{\tilde{z}_k}$ and the error cross covariance$P_{\tilde{x}_k\tilde{z}_k}$. Finally, the kth point error covariance is calculated by using$P_{k|k-1}$, K_k, and $P_{\tilde{z}_k}$.

$$\begin{cases} \widehat{x}_k = \widehat{x}_{k|k-1} + K_k\left(z_k - \widehat{z}_{k|k-1}\right) \\ K_k = P_{\tilde{x}_k\tilde{z}_k} P_{\tilde{z}_k}^{-1} \\ P_k = P_{k|k-1} - K_k P_{\tilde{z}_k} K_k^T \end{cases} \tag{27}$$

4.3. Strong tracking factor is used in STSPKF

The Strong Tracking Factor (STF) can adjust gain matrix online by introducing fading factor to the state estimation covariance matrix.

In order to calculate the fading factor μ_k, residual error ε_k, which is the difference between the measurement data z_k and $k|k-1$ step measurement prediction result $\widehat{z}_{k|k-1}$, and residual error sequence covariance matrix V_k should be defined firstly.

$$\varepsilon_k = z_k - \widehat{z}_{k|k-1} \tag{28}$$

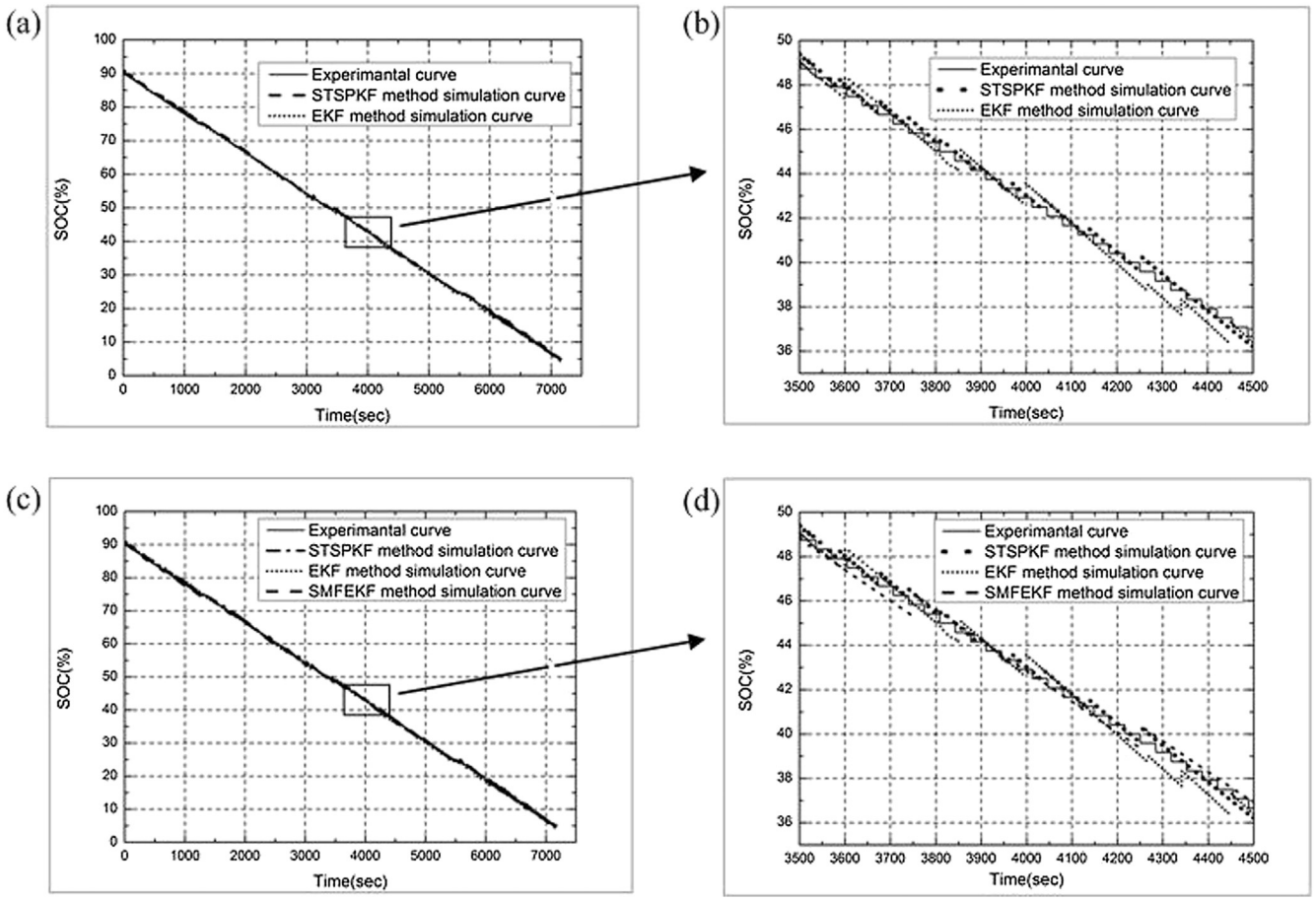

Fig. 10. Comparison between simulation results and experiment data: (a) STSPKF, EKF and experiment data; (b) zoom figure for (a); (c) STSPKF, EKF, SMFEKF and experiment data; (d) zoom figure for (c).

$$V_k = \begin{cases} \varepsilon_1 \varepsilon_1^T & k = 1 \\ \dfrac{\rho V_{k-1} + \varepsilon_k \varepsilon_k^T}{1+\rho} & k \geq 2, 0 \leq \rho \leq 1 \end{cases} \tag{29}$$

Secondly, N_k matrix M_k and are defined in equation (30), which are used for calculating the fading factor μ_k.

$$\begin{cases} N_k = V_k - H_k Q_{k-1} H_k^T - R_k \\ M_k = H_k P_{k|k-1} H_k^T + R_k - V_k + N_k \end{cases} \tag{30}$$

whereH_k is the measure matrix of the equation (11), Q_{k-1} is the system process error matrix, R_k is the measure error matrix, and $P_{k|k-1}$ is the step error covariance.

Finally, the fading factor μ_k is calculated by equation (31).

$$\mu_k = \begin{cases} \mu_0 & \mu_0 \geq 1 \\ 1 & \mu_0 < 1 \end{cases} \tag{31}$$

$$\mu_0 = \frac{tr[N_k]}{tr[M_k]} \tag{32}$$

where $tr[N_k]$ and $tr[M_k]$ are the trace of the matrix N_k and M_k respectively.

The idea of the STF is to make discrepancy orthogonal at each step and get useful information from the discrepancy series as current state estimation. As a result, the STF can keep its tracking ability to the system state variables with system model uncertainty. The equation (33), which containing the fading factor μ_k in the first term of the equation, should replace the equation (21) to achieve tracking mechanism.

$$P_{k|k-1} = \mu_k \sum_{i=0}^{L} W_i^c \left(\gamma_{i,k|k-1} - \hat{x}_{k|k-1}\right)\left(\gamma_{i,k|k-1} - \hat{x}_{k|k-1}\right)^T + Q_{k-1} \tag{33}$$

5. Results and discussions

Using Matlab®, for simulation the STSPKF algorithm is compared with the actual experimental results. The initial values used in the simulation are as follows:

$$X_0 = [0.9 \quad 0.016 \quad 0.208]^T,\ q_0 = 0.1,\ r_0 = 0.1,\ Q_0 = 0.1,\ R_0 = 0.1$$

The simulation and the experimental results are shown in Fig. 10, in which the solid line represents the experimental data and other dash or dot lines represent the simulation results. The digatron BTS was used to obtain the experimental data. The vertical axis represents the *SOC* values from 0% to 100%. The horizontal axis represents the simulation time. The power battery was discharged by withdrawing a total charge of 0.5 C-rate at constant current. It

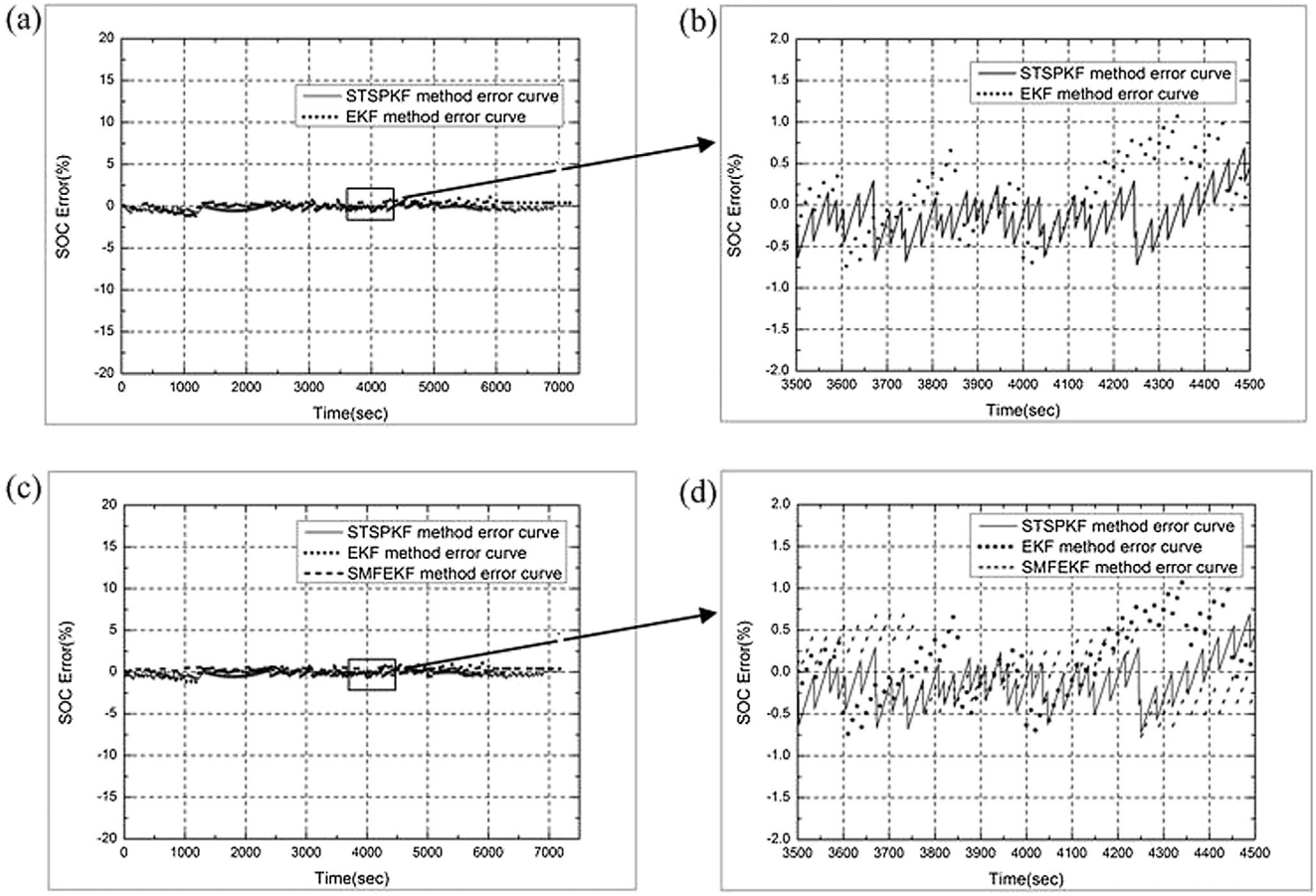

Fig. 11. The error in simulation: (a) the errors in STSPKF and EKF; (b) zoom figure for (a); (c) the error graphs of STSPKF, SMFEKF and EKF; (d) zoom figure for (c).

took less than 2 h for the *SOC* to drop from 90% to 5%.

The simulation results from STSPKF, and EKF methods and the experimental data are compared in Fig. 10(a), while zoom figure for Fig. 10(a) from 3500 s to 4500 s is shown in Fig. 10(b). The qualitative analysis of the results in the graph shows that the error in the EKF method is larger than that of the STSPKF method when compared to the experimental data. The comparison between STSPKF, EKF, Subprime Multiple Fading Extended Kalman Filter (SMFEKF) simulation methods and the experimental data can be seen in Fig. 10(c); zoom figure for Fig. 10(c) is shown in Fig. 10(d) meanwhile. At the simulation, the deviation between the STSPKF and SMFEKF methods is small and negligible when compared to the experimental data. The reason is that both these methods merge the fading factor into the co-variance calculation equation and force the simulation value to track the actual value. The deviation of the EKF method is larger than that of the other two methods due to the lack of tracking mechanism. Overall, the STSPKF method has less simulation error than the EKF and SMFEKF methods as takes into account the STF and adopts weighted statistical linear regression method, which is better than first-order Taylor series to linearize the nonlinear function.

Fig. 11(a) shows the graphs of the errors produced in STSPKF and EKF simulation methods, and Fig. 11(b) shows the errors from 3500 s to 4500 s. The error graphs of STSPKF, SMFEKF and EKF simulation methods' are shown in Figs. 11(c), and Fig. 10(d) shows more clearly. The *SOC* estimation of the battery is more accurate when its actual value is 50% since the electrochemical reaction is sufficient and stable. When the battery charge is near full or empty, the electrochemical reaction is insufficient and unstable. As a result, the side reactions cause inaccuracies to *SOC* estimations.

When the EKF algorithm is used in nonlinear system filtering, the Taylor expansion of first-order linearization cut off is adopted. This brings in a large divergence and error if system model uncertainty exists. Therefore, since SMFEKF algorithm is based on the EKF algorithm, it also inherits the disadvantages of EKF and diverges with the system model uncertainty. However, provided a stable filter, as the SMFEKF algorithm takes into account the strong tracking factor, it maintains the ability to track the changing state variables. Thus, the SMFEKF algorithm has higher reliability and better convergence compared to those of the EKF method. On the other hand, the STSPKF algorithm can use second-order Taylor accuracy to approximate any nonlinear system. Furthermore, the accuracy of the STSPKF is the best of its three methods due to overcomes the theoretical limitations of EKF algorithm effectively.

Table 4 shows the maximum error and Root-Mean-Square Error (RMSE) of the three simulation methods. Obviously, the STSPKF performs better than the other two, and SMFEKF is better than the EKF. In Ref. [55], the authors compared SPKF and EKF simulation methods, the EKF maximum error and RMSE is 1.10% and 0.64% respectively, and the SPKF maximum error and RMSE is 0.90% and 0.49%, which is bigger than this study. It can be concluded that it is possible to increase the accuracy of *SOC* estimation by joining the strong tracking factor to improve the SPKF algorithm.

Table 4
The errors in *SOC* estimations by STSPKF, SMFEKF and EKF methods.

Method	STSPKF	SMFEKF	EKF
Maximum error	0.83%	0.96%	1.18%
RMSE	0.46%	0.58%	0.66%

6. Conclusions

This paper presents the STSPKF algorithm for power battery *SOC* estimation. The STSPKF possesses the higher estimation accuracy by adaptively adjusting the values of the process and measurements' noise co-variances in real time with the help of the STF. A second-order *RC* network *ECM* was used to describe the behavior of $LiMn_2O_4$ power battery, due to it strikes a balance between the model accuracy and computational complexity. The power battery characteristic experiment and test data were obtained to perform parameters identification. Both the experimental as well as simulation results showed that the STSPKF algorithm can estimate the battery *SOC* with higher accuracy comparing with the SMFEKF, and EKF algorithms.

Future work will focus on developing a more accurate battery model to describe the relaxation effect with low computational complexity. A better performance of the *SOC* estimation algorithm can be derived from more accurate battery model. In addition, the battery experiments under more specific conditions should be performed to make the research results is more comprehensive.

Acknowledgments

This research is supported by China Guangdong provincial Strategic emerging industries core technology breakthrough project (2012A010702004).

References

[1] Wei He, Nicholas Williard, Chaochao Chen, Michael Pecht, Microelectron. Reliab. 53 (2013) 840–847.
[2] Fengchun Sun, Xiaosong Hu, Yuan Zou, Siguang Li, Energy 36 (2011) 3531–3540.
[3] Barelli Linda, Bidini Gianni, Ottaviano Andrea. ApplEnergy j.apenergy.2011.11.04.
[4] Y. Ma, Q.S. Chen, Z. Qi, J. Tsinghua Univ. Sci. Tech. 41 (50) (2001) 95–97.
[5] Sabine Piller, Marion Perrin, Andreas Jossen, J. Power Sources 96 (2001) 113–120.
[6] H. Terry, C.J. Wang, J. Power Sources 141 (2005) 351–358.
[7] J.P. Wang, Q.S. Chen, B.G. Cao, Energy Convers. Manage 47 (7) (2006) 858–864.
[8] J.P. Wang, L. Xu, J.G. Guo, L. Ding, J. Automob. Eng. 223 (1) (2009) 27–35.
[9] Wang Junping, Guo Jingang, Ding Lei, Energy Convers. Manag. 50 (2009) 3182–3186.
[10] Reinhardt Klein, Nalin A. Chaturvedi, Jake Christensen, Jasim Ahmed, Rolf Findeisen, Aleksandar Kojic, IEEE Trans. Control Syst. Technol. 21 (2) (2013).
[11] Meng Guo, Gi-Heon Kim, Ralph E. White, J. Power Sources 240 (2013) 80–94.
[12] Quanshi Chen, Chengtao Lin, Veh. Technol. 3 (2005).
[13] E. Karden, S. Buller, R.W. DeDoncker, J. Power Sources 85 (2000) 72e78.
[14] Jun Xu, Chunting Chris Mi, Binggang Cao, Junyi Cao, J. Power Sources 233 (2013) 277–284.
[15] Hans-Georg Schweiger, Ossama Obeidi, Oliver Komesker, André Raschke, Michael Schiemann, Christian Zehner, Markus Gehnen, Michael Keller, Peter Birke, Sensors 10 (2010) 5604–5625.
[16] A. Zenati, Ph Desprez, H. Razik, IECON 5675408 (2010) 1773–1778.
[17] Stephan Buller, Marc Thele, Rik W.A.A. De Doncker, Eckhard Karden, IEEE Trans. Ind. Appl. 41 (3) (2005).
[18] Virgilio Valdivia, Antonio Ĺ azaro, Andŕ es Barrado, Pablo Zumel, Cristina Ferń andez, Marina Sanz, IEEE Trans. Power Electron. 26 (12) (2011).
[19] F. Parigi, Y. Gao, T. Gachovska, J.L. Hudgins, D. Patterson, Y. Lu, in: IEEE Vehicle Power and Propulsion Conference, 2012.
[20] M. Dubarry, B.Y. Liaw, J. Power Sources 174 (2007) 856–860.
[21] C.M. Sheperd, J. Electrochem Soc. 112 (1965) 657.
[22] Y. Hu, S. Yurkovich, Y. Guezennec, B.J. Yurkovich, Control EngPract Theory 15 (2009) 1190.
[23] Lijun Gao, Shengyi Liu, Roger A. Dougal, IEEE Trans. Comp. Packag. Technol. 25 (3) (september 2002).
[24] Kannan Thirugnanam, Himanshu Saini, Praveen Kumar. 2012 IEEE.978-1-4673-1408-4/12.
[25] Sungwoo Cho, Hyeonseok Jeong, Chonghun Hana, Shanshan Jin, Jae Hwan Lim, Jeonkeun Oh, Comput. Chem. Eng. 41 (2012) 1–9.
[26] Low Wen Yao, Aziz, J.A, Ramli, N. IEEE.
[27] Krishnan S. Hariharan, V. Senthil Kumar, J. Power Sources 222 (2013) 210–217.
[28] Hongwen He, Rui Xiong, Hongqiang Guo, Shuchun Li, Energy Convers. Manag. 64 (2012) 113–121.
[29] Tingshu Hu, Hoeguk Jung, J. Power Sources 233 (2013) 14–22.
[30] C.C. Chan, E.W.C. Lo, W. Shen, J. Power Sources 87 (2000) 201–204.
[31] W.X. Shen, C.C. Chan, E.W.C. Lo, K.T. Chau, Energy Convers. Manag. 43 (2002) 817–826.
[32] W.X. Shen, Energy Convers. Manag. 48 (2007) 433–442.
[33] W.X. Shen, K.T. Chau, C.C. Chan, IEEE Trans. on Veh. Technol. 54 (2005) 1705–1712.
[34] Y. Morita, S. Yamamoto, S.H. Lee, N. Mizuno, Asian J. Control 8 (2006) 268–273.
[35] K.T. Chau, K.C. Wu, C.C. Chan, W.X. Shen, Energy Convers. Manag. 44 (2003) 2059–2071.
[36] P. Singh, R. Vinjamu, X.P. Wang, D. Reisne, J. Power Sources 162 (2006) 829–836.
[37] S. Malkhandi, Eng. Appl. Artif. Intell. 19 (2006) 479–485.
[38] J.C. ÁlvarezAntón, P.J. García Nieto, F.J. de Cos Juez, F. Sánchez Lasheras, M. González Vegaa, M.N. Roqueñí Gutiérrez, Appl. Math. Model. 37 (2013) 6244–6253.
[39] Wang Junpinga, Chen Quanshi, Cao Binggang, Energy Convers. Manag. 47 (2006) 858–864.
[40] T. Hansen, C.J. Wang, J. Power Sources 141 (2005) 351–358.
[41] Q.S. Shi, C.H. Zhang, N.X. Cui, Int. J. Automot. Technol. 9 (2008) 759–764.
[42] X.S. Hu, F.C. Sun, in: International Conference on Intelligent Human-machine Systems andCybernetics, 2009, pp. 392–396.
[43] Gregory L. Plett, J. Power Sources 134 (2004) 262–276.
[44] Saeed Sepasi, Reza Ghorbani, BorYann Liaw, J. Power Sources 245 (2014) 337–344.
[45] Jaemoon Lee, Oanyong Nam, B.H. Cho, J. Power Sources 174 (2007) 9–15.
[46] D. Andre, A. Nuhic, T. Soczka-Guth, D.U. Sauer, Eng. Appl. Artif. Intell. 26 (2013) 951–961.
[47] M.R. Mohamed, H. Ahmad, M.N. Abu Seman, S. Razali, M.S. Najib, J. Power Sources 239 (2013) 284–293.
[48] Saeed Sepasi, Reza Ghorbani, BorYann Liaw, J. Power Sources 255 (2014) 368–376.
[49] Rui Xiong, Fengchun Sun, Zheng Chen, Hongwen He, Appl. Energy 113 (2014) 463–476.
[50] Rui Xiong, Xianzhi Gong, Chunting Chris Mi, Fengchun Sun, J. Power Sources 243 (2013) 805–816.
[51] Rui Xiong, Fengchun Sun, Hongwen He, TrongDuy Nguyen, Energy 63 (2013) 295–308.
[52] S.J. Julier, J.K. Uhlmann, Simulation and Controls, 1997, pp. 182–193.
[53] E.A. Wan, R. Van Der Merwe, Communications and Control, 2000, pp. 153–158.
[54] F. Sun, X. Hu, Y. Zou, S. Li, Energy 36 (2011) 3531–3540.
[55] G.L. Plett, J. Power Sources 161 (2006) 1356–1368.
[56] Xiaojun Tan, Electric Vehicle Power Battery Management System Design, Sun Yat-sen University Press, 2011.
[57] "Freedom CAR Battery Test Manual" HPPC Test Standard.
[58] <USABC electric vehicle battery test manual>.
[59] G. Marangoni, University of Padova, 2010.
[60] Hongwen He, Rui Xiong, Jinxin Fan, Energies 4 (2011) 582–598.
[61] R.E. Kalman, Trans. ASME J. Basic Eng. 82 (1960) 35–45.